Research Square

Preprints are preliminary reports that have not undergone peer review.
They should not be considered conclusive, used to inform clinical practice,
or referenced by the media as validated information.

When can an excitonic insulator be a purely electronic ferroelectric? Symmetry conditions tested on monolayer Ta2Pd3Te5

Gabor I. Csonka

csonkagi@gmail.com

Tulane University https://orcid.org/0000-0001-5701-4401

Hong Tang

Tulane University

Adrienn Ruzsinszky

Tulane University

Research Article

Keywords:

Posted Date: November 17th, 2026

DOI: https://doi.org/10.21203/rs.3.rs-11755846/v1

License: This work is licensed under a Creative Commons Attribution 4.0 International License.
Read Full License

Additional Declarations: The authors declare no competing interests.

When can an excitonic insulator be a purely electronic ferroelectric? Symmetry conditions tested on monolayer $Ta_2Pd_3Te_5$

Gábor I. Csonka[1,*], Hong Tang[1] and Adrienn Ruzsinszky[1]

[1]Department of Physics and Engineering Physics, Tulane University, New Orleans, LA 70118, USA
[*]Corresponding author: csonkagi@gmail.com (ORCID 0000-0001-5701-4401)

Abstract

Excitonic condensation could produce ferroelectricity without ionic displacement. We formulate the symmetry conditions such a purely electronic ferroelectric must satisfy and test them on monolayer $Ta_2Pd_3Te_5$, an excitonic-insulator candidate with both band edges at Γ. For spin-singlet pairing the band edges form the nonpolar, chiral A_u order; a polar B_{3u} singlet requires the second conduction band, whereas a time-reversal-even spin-triplet condensate of the band edges would be polar. The maximally localized Wannier Hamiltonian retains only the isotropy group of B_{3u} and cannot separate the polar channel from its competitors; within the symmetry it respects, the channel containing A_u has the lowest critical coupling. For singlet pairing the polar condition conflicts with the excitonic mechanism: dipole-forbidden band edges keep the attraction unscreened and make the order nonpolar. Second-harmonic generation, shear-induced out-of-plane polarization and Raman activation of silent phonons discriminate the orders directly.

Ferroelectricity in solids conventionally arises from ionic displacements that break inversion symmetry. Electronic ferroelectricity (EF) is the distinct case in which electronic degrees of freedom alone produce the polar state. An excitonic insulator[1] provides a natural route: spontaneous electron-hole coherence between bands of opposite parity can shift the electronic centre of charge with the lattice held fixed[2;3]. Established candidates remain scarce. Organic charge-transfer salts[4] show unconventional ferroelectric responses in which lattice contributions are rarely excluded, and graphene moiré superlattices show electronic ferroelectricity carried by electron–hole dipoles, with holes bound by the moiré potential and electrons injected by a gate[5;6]; there the polar state is imposed by an extrinsic potential rather than formed by spontaneous condensation. A recent review sets out general criteria for a pure electronic ferroelectric, among them that the transition proceeds

without lattice distortion or structural symmetry breaking[7]; these criteria do not refer to a specific mechanism.

Here we formulate five conditions specific to the excitonic route. Single ingredients are known: a uniform order requires both band edges at the same wave vector, a polar one requires pairing between bands of opposite parity[2;3], and switchability belongs to the definition of a ferroelectric. Conditions 3 and 4, and the set as a whole, are formulated here.

1. Uniform instability. The order develops at $\mathbf{q} = 0$, which requires both band edges at the same wave vector.

2. Polar order parameter. The product of the paired band representations, $\Gamma_c \otimes \Gamma_v$, contains a vector representation, so that the interband transition is dipole allowed.

3. Dominance. The polar channel is the leading instability, with a lower critical coupling than every competing channel. A calculation can establish this only in a basis that preserves the parent symmetry and therefore separates the channels.

4. Electronic dominance of the polarization. A polar order parameter couples linearly to the polar optical phonons of the same representation, so some ionic displacement always accompanies it. The electronic contribution to the polarization must dominate, and the transition must not be driven by a soft polar phonon. This condition replaces the strict no-distortion criterion, which no polar order satisfies.

5. Switchability. The ordered state is gapped and has two degenerate states $\pm\mathbf{P}$, which follows from conditions 2 and 3 in a centrosymmetric parent.

$TiSe_2$ fails condition 1, since its order develops at a finite wave vector[8;9]. In Ta_2NiSe_5 the $\mathbf{q} = 0$ order breaks the mirrors but preserves inversion[10], failing condition 2, and the relative weight of excitonic and phononic drivers of its transition remains disputed[11–13]. $Ta_2Pd_3Te_5$ is the current focus. The bulk compound crystallizes in $Pnma$[14], becomes insulating on cooling, with a transition reported near 365 K and a fully developed gap below about 100 K, and shows signatures of excitonic order[15–17], and hosts correlated edge states[18]. Its monolayer, with layer symmetry $Pmmn$, is a near-zero-gap semiconductor with both band edges at Γ and an excitonic instability at $\mathbf{q} = 0$[19;20].

The symmetry of the condensate is partly settled. The order parameter of a $\mathbf{q} = 0$ excitonic insulator transforms as the product of the conduction- and valence-band representations. Yao *et al.* showed that the monolayer band edges carry Γ_4^+ and Γ_4^-, so that the band-edge 1s exciton breaks inversion and every mirror[19], and Huang *et al.* obtained a bulk Hartree–Fock order parameter with the same broken symmetries[15]. These are the properties of the nonpolar A_u representation, so the spin-singlet band-edge order fails condition 2. Three questions remain open: whether the Wannier Hamiltonians used in such mean-field calculations can test condition 3 at all, by distinguishing A_u from the polar B_{3u} channel, how the two channels compare in a model restricted to the symmetry it actually has, and which observables separate them. We show that the standard maximally localized Wannier Hamiltonian of the monolayer carries a spurious polar symmetry breaking that merges B_{3u} with the normal state, we derive the instability thresholds of the channels it can separate, and we identify the chiral isotropy groups of the A_u state, their consistency with the bulk observations, and experimental discriminators. Finally, we show that condition 2 conflicts with the excitonic mechanism itself, which yields a design rule for excitonic electronic ferroelectrics.

Results

Bulk structure and excitonic-insulator context

Bulk $Ta_2Pd_3Te_5$ is a van der Waals layered compound crystallizing in the orthorhombic space group *Pnma* (No. 62) with point group *mmm*[14]. Figure 1 shows the layered crystal structure, composed of sheets and ribbons. The quasi-one-dimensional fused $TaTe_5$ chains run along the crystallographic *b* axis, a structural motif that strongly influences the low-energy electronic dispersion.

Electron diffraction gives conflicting evidence for a subtle breaking of the bulk symmetry. Huang *et al.* observe the glide-forbidden (*h*00) and (00*l*) reflections at 300 and 100 K but not at 368 K, close to the metal–insulator transition near 365 K; among the orthorhombic subgroups of *Pnma*, only $P2_12_12_1$ accounts for both[15]. Zhang *et al.* detect weak reflections forbidden in *Pnma* below about 330 K, with the (005) intensity only 2.7% of the (004) intensity[16]. Hossain *et al.* observe the same reflections at 373, 290 and 90 K, essentially unchanged with temperature, and attribute them to multiple scattering in thin lamellae; their X-ray data show no structural transi-

tion[17]. X-ray diffraction does not resolve the distortion[16]: single-crystal data at 300 and 50 K refine well in *Pnma*, the 50 K refinements in *Pnma* and $P2_12_12_1$ show the distortion to be exceptionally small, and the band structure computed in $P2_12_12_1$ is almost unchanged[15]. The calculated phonon spectrum of the *Pnma* structure has no imaginary frequencies[15], and Huang *et al.* and Zhang *et al.* attribute the distortion to the coupling of the lattice to the excitonic order rather than to a lattice instability[15;16]. All three groups agree that lattice involvement is very weak. We therefore use the centrosymmetric *Pnma* structure[14;21] as the parent phase: it is the high-symmetry reference against which the symmetry of the electronic order parameter is classified, and the observed $P2_12_12_1$ distortion is the lattice response to that order.

Bulk $Ta_2Pd_3Te_5$ is an established excitonic-insulator candidate. Transport and ARPES show a metal–insulator transition near 350–365 K and a gap of 55 meV at 75 K that opens from a Dirac-type band crossing at Γ[15;16], whereas scanning tunnelling spectroscopy, transport and specific heat place the opening of the full gap near 100 K[17]; Raman scattering shows both scales[22]. Hossain *et al.* identify a topological excitonic insulator with gapless boundary modes and two condensates, a primary one at zero momentum and a secondary one at finite momentum whose wave vector is tuned by a magnetic field, both breaking mirror symmetry[17]. Density functional calculations with PBE, the modified Becke–Johnson potential, and DFT+U up to 3 eV find the bulk semimetallic and do not account for the insulating ground state[15;21]. r^{2}SCAN[23], the functional used in this work, reproduces with the rVV10 dispersion correction[24] the normal-state bulk dispersion measured by ARPES at 350 K (Fig. S1).

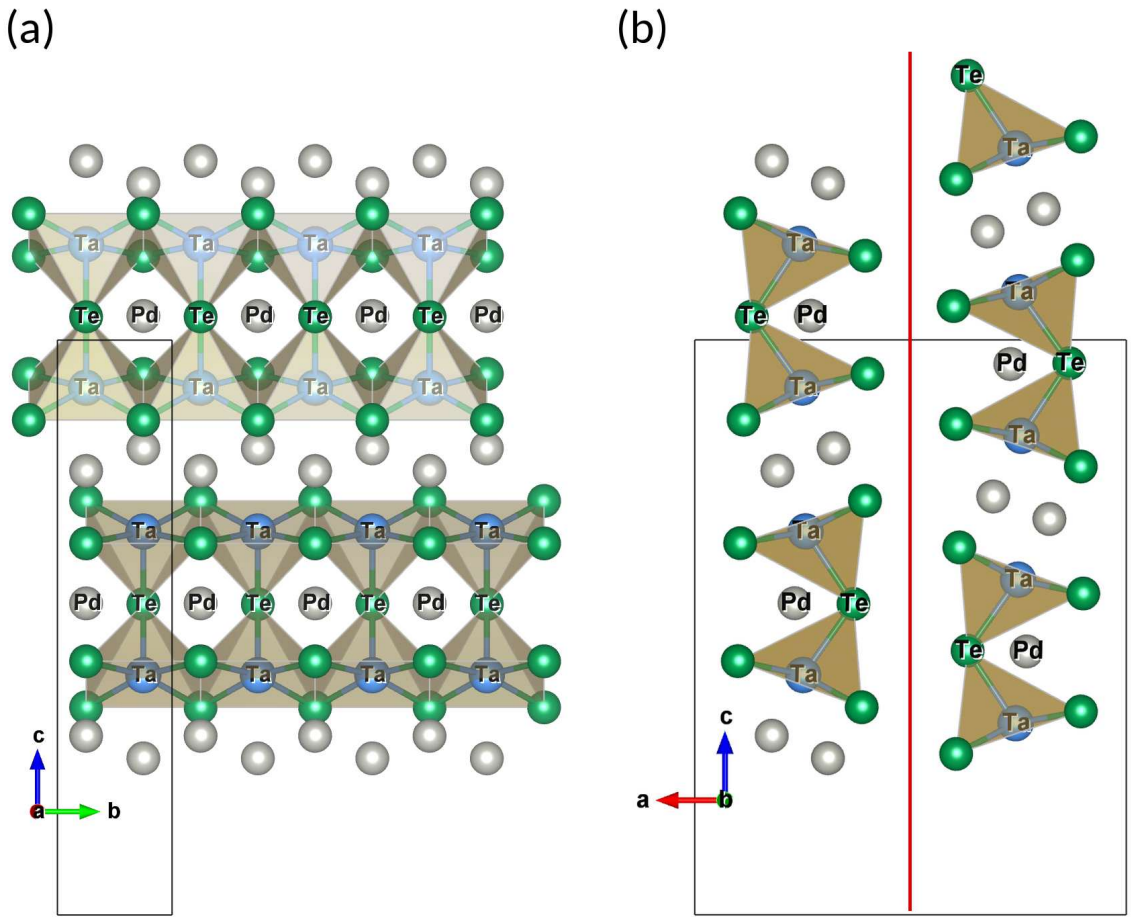


Fig. 1. Crystal structure and coordination projections of bulk $Ta_2Pd_3Te_5$ in the centrosymmetric *Pnma* space group. Ta, Pd, and Te atoms are shown as blue, silver, and green spheres. The structure is two-dimensional and consists of two $Ta_2Pd_3Te_5$ sheets per unit cell. There are two, three, and five inequivalent Ta, Pd, and Te sites, respectively, all on Wyckoff 4*c* positions. (a) Projection along the *a* axis of four unit cells along *b* in the *bc* plane; the second, bottom layer along *a* is omitted here and included in (b). Panel (a) shows the ribbons formed by the fused, distorted rectangular Te_5 pyramids along *b*, the 10-coordinate environment of the two inequivalent Ta sites bonded to five Pd and five Te atoms, and the distinct 8-coordinate (Pd1) and 9-coordinate (Pd2, Pd3) environments of the three independent Pd sites. (b) Projection along the *b* axis (*ac* plane), showing the cross-section of the two-dimensional sheets, their stacking, and a side view of the ribbons formed by the fused Te_5 pyramids; the vertical red line marks the separation of the two sheets. Both panels share the vertical (*c*) scale, so the unit-cell outlines and atomic rows align. Structures rendered with VESTA[25].

Monolayer structure

Figure 2 shows monolayer $Ta_2Pd_3Te_5$ relaxed with r^{2}SCAN ($a = 3.753$ Å, $b = 18.668$ Å). The periodic slab has space group *Pmmn* (No. 59). The monolayer keeps the quasi-one-dimensional Ta–Te chains of the bulk, which now run along a, and contains a single sheet per cell with no interlayer stacking. Its 20 atoms occupy six inequivalent sites: Ta, Pd_B, Te_{B1} and Te_{B2} on fourfold positions on the σ_x mirror planes, and Pd_A and Te_V on twofold positions where the σ_x and σ_y planes intersect. Each Ta is ten-coordinate, as in the bulk. Five Te atoms form a distorted rectangular pyramid with

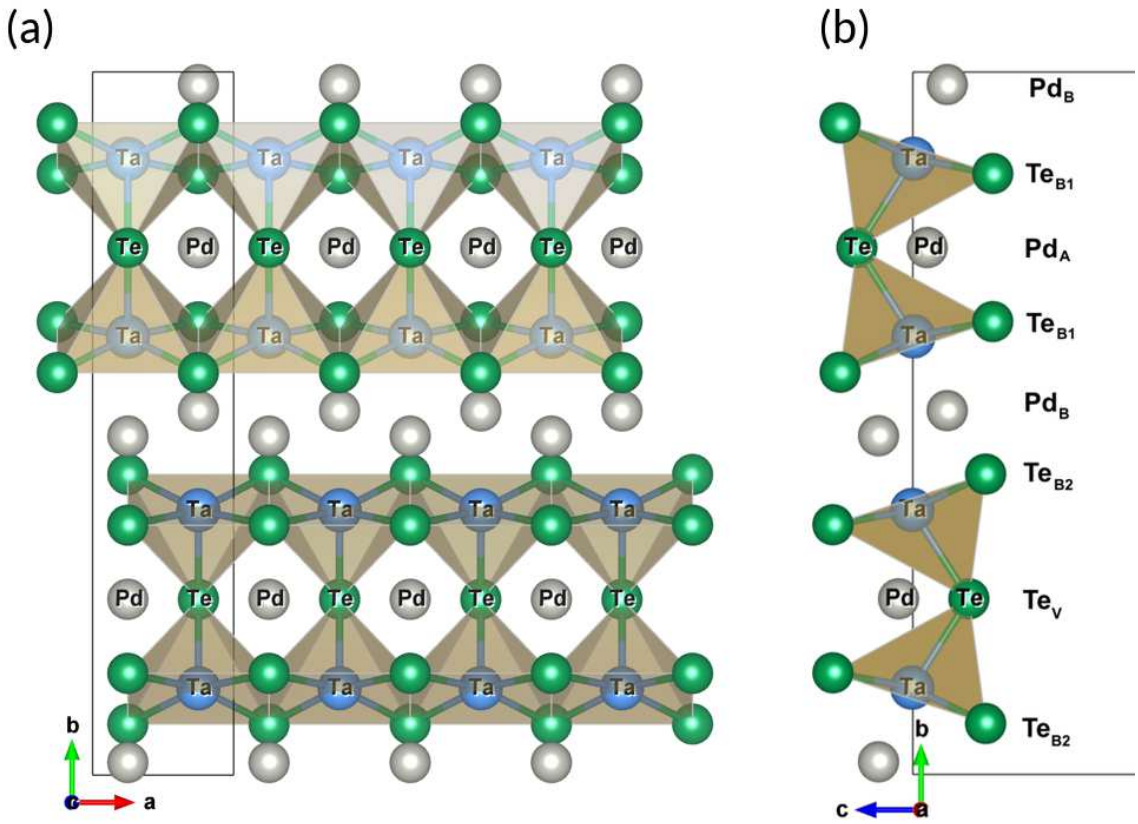


Fig. 2. Relaxed structure of monolayer $Ta_2Pd_3Te_5$ (r^{2}SCAN, space group *Pmmn*). Ta, Pd, and Te atoms are shown as blue, silver, and green spheres. (a) Top view in the *ab* plane of four unit cells along *a*; the rectangle marks one unit cell. The Ta–Te chains formed by distorted $TaTe_5$ rectangular pyramids run along *a*, and Pd_B atoms occupy the channels between the ribbons. (b) Side view in the *cb* plane (projection along *a*) of one unit cell, with *b* vertical on the same scale as (a) so that the atomic rows align. Labels mark the inequivalent sites: the basal Te_{B1} and Te_{B2}, the apical Te_V shared by two pyramids, Pd_A at the centre of each pyramid pair, and Pd_B. Ta lies 0.29 Å outside the basal plane toward Te_V (trans Te_B–Ta–Te_B angle 168.4°), and Ta–Pd_A is 3.04 Å. Structures rendered with VESTA[25].

the apical Te_V at 2.80 Å and the basal Te_B at 2.85 and 2.87 Å, and five Pd atoms complete the shell (Ta–Pd_B 2.80 and 2.87 Å, Ta–Pd_A 3.04 Å). Ta lies 0.29 Å outside the basal plane toward the apex, giving a trans Te_B–Ta–Te_B angle of 168.4°. Two pyramids share each apical Te_V, and Pd_A sits at the centre of the pair, bonded to Te_V at 2.65 Å and to two basal Te at 2.63 Å. The Pd_B atoms occupy the channels between neighbouring ribbons.

Band-edge symmetry and candidate order parameters

Figure 3 shows the bands of the 16-orbital Wannier Hamiltonian near the gap, and Table I lists the Γ-point symmetry eigenvalues of the valence-band maximum v_1 and the two lowest conduction

Table I. Γ-point symmetry eigenvalues of the relevant bands of monolayer $Ta_2Pd_3Te_5$ and the resulting order-parameter irreps. The columns C_{2z}, M_y and I and the band irreps are from ref. 19. The columns 2_{1x}, σ_y and n_z are computed in this work with the exact operations of H_0; for all three bands they agree with the values implied by ref. 19 to 10^{-6}.

State	Irrep	C_{2z}	M_y	I	2_{1x}	σ_y	n_z	Character
v_1	Γ_4^+	-1	$+1$	$+1$	-1	$+1$	-1	valence-band maximum
c_1	Γ_4^-	-1	-1	-1	-1	-1	$+1$	conduction-band minimum
c_2	Γ_2^-	$+1$	$+1$	-1	-1	$+1$	-1	second conduction band
$c_1 \otimes v_1$	A_u	$+1$	-1	-1	$+1$	-1	-1	nonpolar, chiral
$c_2 \otimes v_1$	B_{3u}	-1	$+1$	-1	$+1$	$+1$	$+1$	polar along x

bands c_1 and c_2[19]. Both band edges carry $C_{2z} = -1$, so the band-edge coherence

$$\Gamma_{c_1} \otimes \Gamma_{v_1} = \Gamma_4^- \otimes \Gamma_4^+ = A_u \tag{1}$$

is odd under inversion and every mirror but even under all twofold rotations. It is nonpolar. A polar order along the chain axis requires B_{3u}, which arises only from coherence between c_2 (Γ_2^-) and v_1; the corresponding interband dipole is finite along x and vanishes along y[19]. Our Wannier Hamiltonian reproduces this selection rule [Fig. 3(b)]: the c_2–v_1 velocity matrix element along x is finite at Γ, while the c_1–v_1 element vanishes at Γ and along the entire Γ–X line. Band-edge pairing therefore selects A_u, and B_{3u} is a higher-lying channel whose coherence involves a band that is not at the gap edge. This assignment restates the result of Yao *et al.* that the band-edge 1s exciton breaks inversion and every mirror[19]; we take it as the starting point. The right-hand columns of Table I add the eigenvalues under the operations that our Wannier Hamiltonian respects exactly (see the Wannier-symmetry section), including those of c_2, which lies 103 meV above c_1 in the DFT bands (129 meV in the Wannier model). Under these operations $c_2 \otimes v_1$ has every character equal to $+1$, the same as the fully symmetric representation, which anticipates the merging of B_{3u} with the normal state found below.

Isotropy groups and experimental signatures

Condensation in A_u retains the identity, C_{2z} and the two screws, and removes inversion, both mirrors and the glide. The isotropy layer group is $P2_12_12$, which is chiral and nonpolar. Condensation in B_{3u} retains 2_{1x}, σ_y and n_z, giving a polar group of $Pmn2_1$ type with the polar axis along the

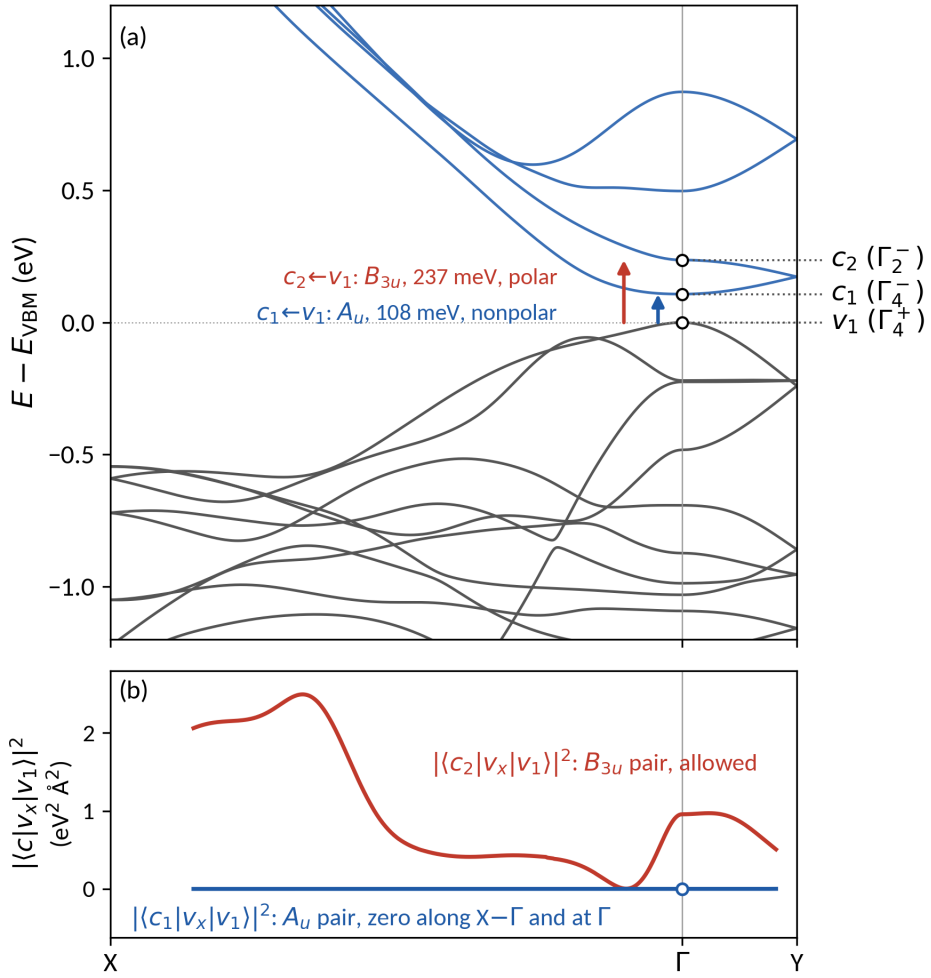


Fig. 3. Band-edge states and interband dipoles of the 16-orbital Wannier Hamiltonian H_0 (r^{2}SCAN) along X–Γ–Y. X lies along the chain direction and Y perpendicular to it; the Γ–Y segment is short because $b = 18.67$ Å. (a) Bands referenced to the valence-band maximum E_{VBM}; grey lines are the 12 occupied bands and blue lines the 4 empty bands. Open circles mark the three Γ-point states that enter the excitonic channels, labelled in the right margin with their irreducible representations (ref. 19): v_1 (Γ_4^+) is the valence-band maximum, c_1 (Γ_4^-) the conduction-band minimum, and c_2 (Γ_2^-) the second conduction band. The blue arrow marks the band-edge pairing $c_1 \leftarrow v_1$, which forms the nonpolar A_u channel across the direct gap of 108 meV in the model (130 meV in DFT); the red arrow marks the pairing $c_2 \leftarrow v_1$, which forms the polar B_{3u} channel at 237 meV (233 meV in DFT). (b) Squared interband velocity matrix elements along the chain, $|\langle c|v_x|v_1\rangle|^2$, with $v_x = \partial H_0/\partial k_x$, for the bands that are v_1, c_1 and c_2 at Γ, followed by eigenvector continuity after near-degenerate states are separated by the operations exact at each $\mathbf{k}$. The c_2–v_1 element (red) is finite at Γ, 0.96 eV^2 Å^2: the polar pair is dipole allowed. The c_1–v_1 element (blue) vanishes along the whole X–Γ line and at Γ, because v_1 and c_1 have opposite σ_y parity: the band-edge pair is dipole forbidden. Curves are omitted within 0.12 Å^{-1} of X, where the followed valence band lies among three near-degenerate bands, and next to Y, where bands meet. Magnitudes are approximate because $\partial H_0/\partial k$ omits intra-cell position matrix elements; the zeros are exact by symmetry.

chains. The two states have sharply different observable consequences (Table II). The A_u exciton is optically dark, whereas the B_{3u} exciton is bright for light polarized along x. At normal incidence with in-plane fields, point group 222 admits only the tensor elements $\chi^{(2)}_{xyz}$ and their permutations,

Table II. Symmetry consequences of the two inversion-odd excitonic channels of monolayer $Ta_2Pd_3Te_5$. The optical selection rule for the A_u exciton follows ref. 19; the bulk structure is that refined in ref. 15.

Property	A_u (band edge)	B_{3u}
Isotropy layer group	$P2_12_12$ (chiral)	$Pmn2_1$ type, polar axis x
Spontaneous polarization	none	P_x
Exciton optical activity	dark	bright, $\mathbf{E} \parallel x$
Normal-incidence in-plane SHG	forbidden	allowed
Response to shear ε_{xy}	$P_z \propto \eta\,\varepsilon_{xy}$	secondary P_y
Γ phonons of the same irrep	four, silent in IR and Raman	five optical, IR active
Same phonons below T_c	Raman active (A of 222), parallel polarizations	IR and Raman active (A_1 of $mm2$)
Bulk counterpart in $Pnma$	$P2_12_12_1$ (observed[15])	not observed

so second-harmonic generation vanishes; point group $mm2$ with polar axis x admits $\chi^{(2)}_{xxx}$, $\chi^{(2)}_{xyy}$ and $\chi^{(2)}_{yxy}$, so it does not[26]. On a substrate the A_u phase reduces to C_2 about the layer normal, which still forbids in-plane second-harmonic generation at normal incidence, while the B_{3u} phase reduces to C_s, which allows it. Because $A_u \otimes B_{1g} = B_{1u}$, an A_u condensate of amplitude η converts an in-plane shear strain ε_{xy} into an out-of-plane polarization $P_z \propto \eta\,\varepsilon_{xy}$, while it carries no spontaneous polarization at any order in η alone. Piezoresponse force microscopy resolves out-of-plane polarization in two-dimensional ferroelectrics such as α-In_2Se_3[27]; in monolayer $Ta_2Pd_3Te_5$ the signature of the A_u order is a shear-induced piezoresponse that appears below the transition and vanishes above it, with no remanent polarization to switch. Below T_c the four silent A_u phonons become fully symmetric A modes of 222 and therefore Raman active in parallel polarizations, with intensity proportional to the square of the lattice distortion.

The bulk data are consistent with the A_u channel. Huang *et al.* observe forbidden $(h00)$ and $(00l)$ reflections below the transition and refine the 50 K structure in $P2_12_12_1$, which removes both glides of $Pnma$[15]. Their Hartree–Fock order parameter breaks inversion and all mirrors[15]. $P2_12_12_1$ is precisely the isotropy group of an A_u order parameter at Γ in $Pnma$, and Hossain *et al.* list it among the subgroups compatible with the mirror breaking they detect[17]. They measure the breaking of one mirror, M_y, in polarization-dependent ARPES and infer a second, M_x, from the low-temperature hybridization of two bands with opposite calculated M_x parity[17]. Each polar representation of D_{2h} breaks exactly one mirror, whereas A_u breaks all three, so two broken mirrors exclude every polar order parameter that transforms as a single irreducible representation;

a polar state would require two coexisting order parameters. Because the diffraction evidence for the distortion itself is disputed (see the bulk-structure section), these bulk observations establish consistency with A_u order rather than a determination of it.

Symmetry content of the Wannier Hamiltonian

A quantitative ranking of A_u and B_{3u} requires a Hamiltonian that respects the full $Pmmn$ group. Table III lists the residuals r_g of the maximally localized H_0. Three operations are exact to within 4.4 meV: the screw 2_{1x}, the mirror σ_y and the glide n_z. The other four, C_{2z}, I, σ_x and 2_{1y}, are violated by 0.53 eV, and for each of them the geometric map sends a Te p_x function onto a Pd d_{xz} function. The origin is visible in the Wannier centres (Fig. 4). An independent symmetry analysis of the centres alone gives space group $Pmn2_1$ (No. 31) for the Wannier centres and $Pmmn$ for the atoms, the same subgroup. Every atom lies on a σ_x plane, so an orbital that is odd or even under σ_x must have its centre on that plane. The Ta d_{z^2} centres lie within 0.03 Å of their planes, but the Te p_x centres are displaced by 0.15 and 0.30 Å. On the σ_y planes at $y = 0$ and $y = b/2$, a Te p_x and a Pd d_{xz} function have hybridized into a pair displaced by 0.65–0.75 Å in opposite directions. The displacement from the mirror planes reflects the character of these functions (Fig. 4). The ten functions seeded as Te p_x have spreads of 10.0–10.8 Å^2 (rms radii of 3.2–3.3 Å), against 5.3 Å^2 for Ta d_{z^2}. They extend over Te–Pd–Te units, and their centres lie 1.7–2.4 Å from the seed atoms and 0.65–1.4 Å from the nearest Pd, within their own rms radius. The basis therefore consists of extended Pd–Te hybrids carrying Te p_x labels, a consequence of disentangling 16 functions from a 6.8 eV window with Te p_x and Pd d_{xz} guides only; nothing in the lattice moves. The Ta d_{z^2} centres stay within 0.24 Å of their atoms. The symmetry is lost already in the disentanglement, which selects the 16-dimensional subspace without a symmetry constraint[28]: projection-only Wannier functions built on the same subspace, without maximal localization, break the same four operations, and raising the frozen window to include c_2 lowers the symmetry further, because at Γ that window contains two states of one irreducible representation while the 16-function basis carries only one (Supporting Information, Sec. S4). Only a disentanglement constrained by the site symmetry[29] restores all eight operations. Because these functions no longer belong to individual atoms, no assignment to parent sites restores $Pmmn$, and a symmetric Hamiltonian cannot be obtained from

Table III. Symmetry residuals r_g of the maximally localized Wannier Hamiltonian H_0 for the seven nontrivial operations of $Pmmn$ (Methods). Operations with r_g below the 20 meV threshold are exact; together with E they form $\{E, 2_{1x}, \sigma_y, n_z\}$, the isotropy group of a B_{3u} order.

Operation	Type	r_g (meV)	Status
n_z	glide, translation $(a/2, b/2, 0)$	3.9	exact
σ_y	mirror	3.5	exact
2_{1x}	screw along the chain	4.4	exact
σ_x	mirror	530.6	broken
I	inversion	530.5	broken
C_{2z}	rotation	530.5	broken
2_{1y}	screw	530.5	broken

this one by averaging over the group.

The four operations that pass the test, $\{E, 2_{1x}, \sigma_y, n_z\}$, form a group isomorphic to C_{2v}, which is exactly the isotropy group of B_{3u}. The normal-state Hamiltonian in this gauge is therefore already polar along the chain axis. Two consequences follow. First, the D_{2h} irreps merge pairwise: A_g and B_{3u} both reduce to A_1 of C_{2v}, and A_u and B_{3g} both reduce to A_2. No projector built on this H_0 separates B_{3u} from the normal state or A_u from B_{3g}. Second, a Wannier-centre or Berry-phase polarization[30] evaluated from this H_0 contains a spurious P_x of gauge origin. Projecting onto excitonic channels with the operators of the ideal $Pmmn$ structure therefore feeds the normal-state hybridization into the order parameter and can produce a polar state that is an artefact of the gauge.

Instability thresholds of the merged channels

Within the exact subgroup, the analysis of Methods yields the critical couplings in Fig. 5. The channel containing A_u has the lowest critical coupling of the four merged channels for every bond cutoff, with V_0^c 9–13% below that of the channel containing B_{3u} and 22–30% below the two remaining channels. All thresholds decrease as more bonds are admitted, because the larger operator space raises $\lambda_{\max}(\chi)$, and all lie above $V = 1.1$ eV, the interaction with which Huang *et al.* obtain the bulk excitonic gap in Hartree–Fock[15]. Below V_0^c the self-consistent field converges to $\boldsymbol{\lambda} = 0$ from every starting guess. The ordering is the same in all four Wannier models of Supporting Information Table S1: the channel containing A_u has the lower critical coupling in each. In the symmetry-adapted model, in which all eight operations are exact and every channel separates,

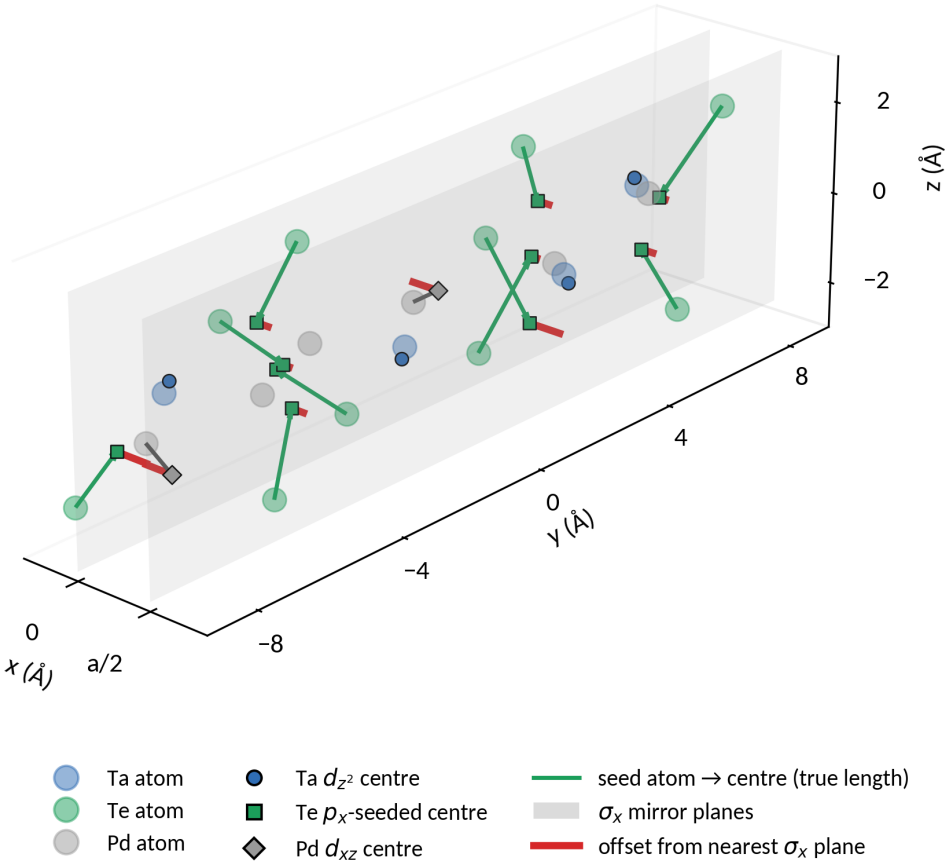


Fig. 4. Wannier centres of the maximally localized Hamiltonian H_0 in one cell of the monolayer, in perspective at true proportions (x along the chains, z normal to the layer). Translucent spheres are atoms (Ta blue, Te green, Pd grey); solid symbols are Wannier centres (circles Ta d_{z^2}, squares Te p_x-seeded, diamonds Pd d_{xz}). Arrows, drawn at true length, run from each projection seed atom to the centre of the resulting function. The ten Te-seeded centres lie 1.7–2.4 Å from their seeds, pulled from the outer Te layers toward the Pd–Te bonds near the mid-plane; these functions are extended Pd–Te hybrids with rms radii of 3.2–3.3 Å, larger than the offsets, so the arrows mark the centres of extended functions, not displacements of anything in the lattice. The Pd centres lie 0.78 Å from their seeds, and the Ta centres 0.24 Å (no arrow drawn). Grey planes are the σ_x mirror planes at $x = 0$ and $x = a/2$, on which every atom lies; a function that is even or odd under σ_x must have its centre on one of them. Red segments mark the offset of each centre from its nearest σ_x plane: the Ta centres lie on the planes, while the Te-seeded and Pd centres lie up to 0.75 Å off them, which breaks σ_x and with it I, C_{2z} and 2_{1y} (Table III). A rotatable version with hover values and switchable layers is provided as Supplementary File S1.

$V_0^c(A_u) = 1.39$ eV (its time-reversal-odd part; the ordinary singlet follows at 1.41 eV) is the lowest, followed by B_{2g} (1.43 eV), B_{1g} (1.90 eV), B_{3u} (1.99 eV) and B_{3g} (2.51 eV); the two lowest channels are both nonpolar as spin-singlet orders, and the polar B_{3u} singlet comes fourth. That model lacks a frozen window and is semimetallic, with band edges 30–140 meV from the DFT values, so it separates the A_u channel from the polar singlet but fixes neither the thresholds nor the order of

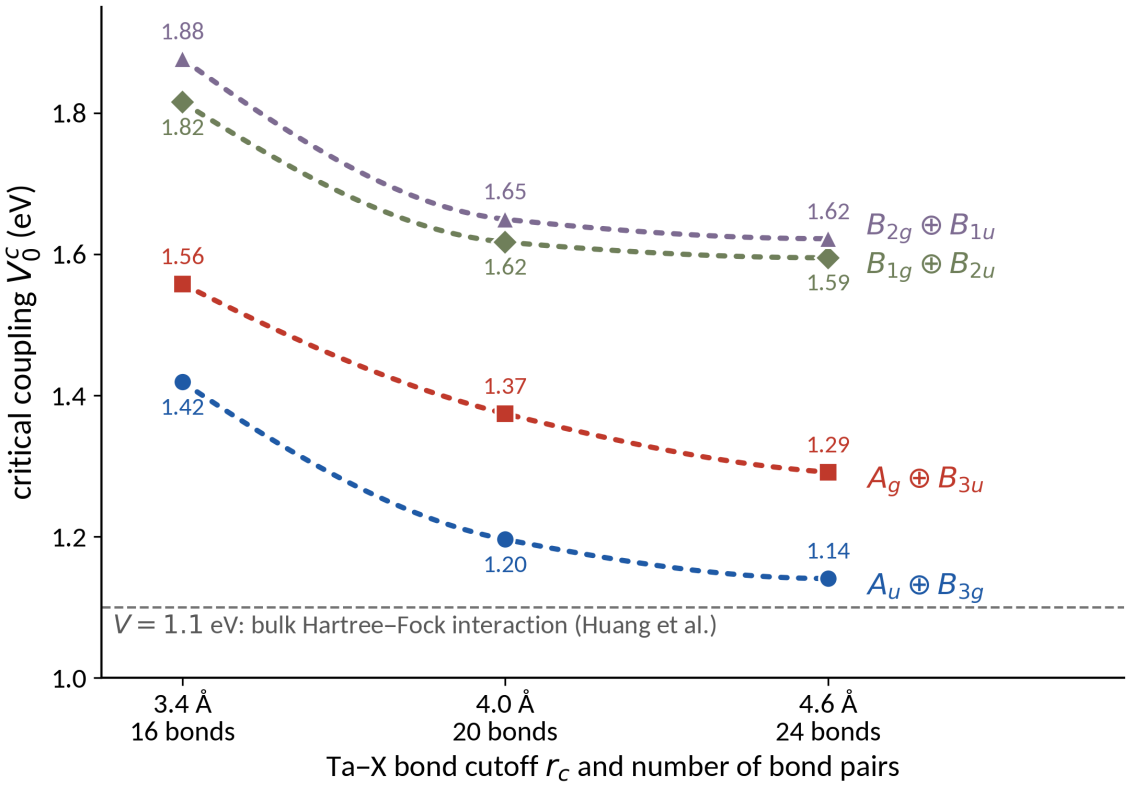


Fig. 5. Critical coupling V_0^c of the four merged excitonic channels that the Wannier Hamiltonian can separate, as a function of the Ta–X bond cutoff r_c; the tick labels give r_c and the number of bond pairs included. Blue circles: $A_u \oplus B_{3g}$, which contains the band-edge A_u order. Red squares: $A_g \oplus B_{3u}$, which contains the polar B_{3u} order. Green diamonds: $B_{1g} \oplus B_{2u}$. Purple triangles: $B_{2g} \oplus B_{1u}$. Each marker is $1/\lambda_{\max}$ of the channel pair susceptibility on a 36×8 mesh, with its value in eV; the dotted curves are monotone interpolants through these values and guide the eye. All thresholds fall as bonds are added because the larger operator space raises $\lambda_{\max}$, and the A_u-containing channel has the lowest critical coupling at every cutoff. The dashed line marks $V = 1.1$ eV, the interaction of the bulk Hartree–Fock model of ref. 15; all four channels lie above it.

the three lowest channels, which lie within 3%. The precise thresholds await a model that is both symmetric and correct at the band edges, which requires a symmetry-constrained disentanglement with a frozen energy window.

Discussion

Two results identify A_u as the natural excitonic order of monolayer $Ta_2Pd_3Te_5$. Group theory fixes the band-edge coherence to A_u (ref. 19), and within the Wannier model the channel that contains A_u becomes unstable first (Fig. 5). The first result is exact and independent of any model. The second depends on the Wannier model and ranks merged channels: the channel with the lower

critical coupling contains both A_u and B_{3g}, so it shows that this channel becomes unstable before the polar one; the symmetry-adapted model, in which A_u and B_{3g} separate, places A_u at 1.39 eV, well below B_{3g} at 2.51 eV, the order proposed from Raman data[22]. The bulk observations support this assignment without establishing it, because they concern the stacked three-dimensional crystal rather than the monolayer and the diffraction evidence is disputed: the mirror breaking detected by ARPES excludes every single-irrep polar order, and the $P2_12_12_1$ distortion, where present, is the A_u isotropy group (see the isotropy-group section).

$Ta_2Pd_3Te_5$ has Γ-point phonons of A_u symmetry; in the monolayer, the four fourfold Wyckoff sets each contribute one x-polarized A_u mode, silent in both infrared and Raman spectra. An A_u excitonic order parameter η and an A_u lattice coordinate u form the invariant ηu, so condensation of either induces the other linearly, as for the excitonic order of Ta_2NiSe_5[10]. Because ηu is bilinear, η and u form a single order parameter, and which of them drives the transition is a quantitative question. An A_u excitonic transition is therefore necessarily accompanied by a lattice distortion of the same symmetry, consistent with the very weak lattice involvement found in all bulk experiments[15–17]. With the electronic thresholds above the 1.1 eV interaction that yields the bulk gap in Hartree–Fock[15], electron-phonon coupling through these modes is the likely ingredient that drives the transition. This lattice response is not specific to the nonpolar channel: a B_{3u} order couples in the same way to the five B_{3u} optical phonons, which is why condition 4 replaces the strict no-distortion criterion of ref. 7. Local probes test condition 4 directly: in Ta_2NiSe_5, scanning tunnelling spectroscopy finds the insulating gap unchanged at structural domain boundaries where the lattice distortion is absent[13], and the same measurement at domain boundaries of the low-temperature phase would separate the electronic gap of $Ta_2Pd_3Te_5$ from its A_u lattice response. It also qualifies the conclusion of ref. 19 that the monolayer is an excitonic insulator without structural distortion: the dynamical stability of the normal state does not prevent the linear coupling of the condensate to the A_u lattice modes.

With spin, each Γ state of $Pmmn$ is a Kramers doublet of the double group, and $\Gamma_5^- \otimes \Gamma_5^+ = A_u \oplus B_{1u} \oplus B_{2u} \oplus B_{3u}$. The A_u component is the spin-singlet order analysed here; in the maximally localized model its leading eigenvector is time-reversal even at every cutoff, an ordinary excitonic order rather than a bond-current state. The others are spin-triplet orders, A_u times the spin axial

vector. A real triplet amplitude is odd under time reversal and is magnetic; an imaginary one is even, carries spin currents[31;32], and its B_{3u} component, A_u times S_x, is polar along the chains, with a polarization that arises only through spin–orbit coupling[33]. A density–density interaction leaves singlet and triplet degenerate for the same orbital amplitude: the ordinary singlet with the magnetic triplet, and a bond-current singlet with the polar spin-current triplet, whose threshold is therefore that of the time-reversal-odd part of the A_u channel. In the maximally localized model that part lies 9–13% above the ordinary singlet; in the symmetry-adapted model it is the lowest instability of all channels, 1.39 eV against 1.41 eV for the ordinary singlet, so the present models do not decide which of the two leads. Three effects the model omits decide between them: electron–hole exchange, which raises the singlet; spin–orbit coupling, which splits the triplet components and mixes the B_{3u} triplet with the singlet c_2–v_1 B_{3u} pair; and pair hopping, which further separates the magnetic from the polar triplet. Condition 2 therefore fails at the band edges for spin-singlet pairing; a time-reversal-even triplet condensate would satisfy it and is not excluded by symmetry.

A polar spin-singlet B_{3u} state is not excluded by symmetry, but it is not the band-edge instability. It requires coherence with c_2, which lies above the conduction-band minimum, and the merged channel that contains it has the higher critical coupling in every model we examined. The depolarization field supplies no additional penalty on a uniform, single-domain state: for in-plane polarization of an infinite monolayer ($\mathbf{q} = 0$) it vanishes, and stray fields arise only at domain boundaries, for longitudinal modulations at finite $\mathbf{q}$, and at dielectric interfaces.

Measured against the five conditions, monolayer $Ta_2Pd_3Te_5$ meets condition 1, fails condition 2 at the band edges for spin-singlet pairing, and leaves condition 3 untested in the available basis; within the symmetry the Wannier Hamiltonian respects, the channel containing B_{3u} has the higher critical coupling. The failure of condition 2 is not an accident of this material. Yao *et al.* traced the excitonic instability of the monolayer to the common symmetry of the band edges, which keeps the two-dimensional polarizability finite as the gap closes[19]. Dipole-allowed band edges, which condition 2 requires, make the polarizability grow as the gap closes; the binding energy then follows the usual two-dimensional scaling $E_b \approx E_g/4$[19] and stays below the gap. The selection rule that favours condensation therefore disfavours a polar condensate; Fig. 3(b) shows both sides of it in one material, a dark band-edge pair and a bright polar pair 103 meV higher. The same ordering

appears in the isostructural $Ta_2Ni_3Te_5$ monolayer, where GW+BSE places the lowest, dark exciton ($v_1 \rightarrow c_1$) about 66 meV below the first bright exciton, which involves the second conduction band[34]. A purely electronic excitonic ferroelectric requires either a polar band-edge pair whose interband dipole is weak but nonzero, small enough to leave the attraction unscreened and large enough to make the order polar, or a polar channel that becomes the leading instability away from the band edges, as the c_2–v_1 channel here would if c_2 dropped below c_1. A spin-triplet band-edge exciton is a candidate of the first kind: spin-forbidden and therefore dark, it keeps the attraction unscreened, and spin–orbit coupling gives it a small dipole along the chains. Whether it condenses before the singlet is an energetic question that symmetry cannot settle; GW+BSE calculations with spin–orbit coupling at $\mathbf{q} = 0$, which give the double-group symmetry and the singlet or triplet character of the lowest excitons, are the decisive test. Band-edge irreps and interband dipole matrix elements screen candidates for the first two conditions directly; condition 3 must then be checked in a symmetry-preserving basis.

Raman scattering provides a bulk test. Each sheet of the $Pnma$ cell keeps only four operations (the identity, the 2_1 screw along c, the mirror perpendicular to b and the glide perpendicular to a), and the two stackings of the monolayer A_u order are the A_u and B_{1g} representations of $Pnma$. Choi *et al.* assign the bulk order parameter to B_{3g}, adopting calculations for Ta_2NiSe_5[10;22]. The Ta_2NiSe_5 order breaks the mirrors but preserves inversion[10], whereas the band edges of $Ta_2Pd_3Te_5$ have opposite inversion parity[17;19], so the order here is inversion-odd and B_{3g} is not a stacking of it. The amplitude mode of an A_u condensate is fully symmetric in the ordered phase and appears in parallel polarizations, where Choi *et al.* observe their A1 and A2 features growing below T^*[22]. The ten silent A_u phonons of the bulk, one per $4c$ site, as in the Γ-point decomposition of isostructural $Ta_2Ni_3Te_5$[35], become Raman active in parallel polarizations below the transition, with intensity proportional to the square of the distortion. Backscattering from the cleaved surface accesses only A_g and B_{3g} modes[35;36], and temperature-dependent spectra of ten-layer $Ta_2Pd_3Te_5$ between 80 and 300 K resolve no new modes but show anomalies in peak positions and linewidths near 150 K[36]; together with the modes resolved in ref. 22, this is consistent with a transition of weak lattice involvement and the very small distortion.

Three measurements discriminate between the channels directly. Normal-incidence second-

harmonic generation with in-plane polarization vanishes in the A_u phase and is allowed in a B_{3u} phase, the A_u phase converts in-plane shear into an out-of-plane polarization, and the silent A_u phonons become Raman active in parallel polarizations below the transition (Table II). Both apply equally to the bulk $P2_12_12_1$ phase.

The quantitative separation of A_u from B_{3g} and of B_{3u} from A_g requires a Wannier basis that respects all of $Pmmn$. Symmetry-adapted Wannier functions[29] cannot be generated through the Wannier90 site-symmetry route from VASP output, which lacks the required symmetry data, and with Quantum ESPRESSO input that route excludes the frozen window that fixes the band edges, so the symmetric model of Supporting Information Table S1 misses them by 30–140 meV. The site-symmetry method[29] combined with a frozen window is implemented in WannierBerri with IrRep[37;38]. Applied to a symmetric Hamiltonian, the present code detects all eight operations as exact and returns separate A_u and B_{3u} thresholds without modification (Supporting Information, Table S1).

We have formulated five conditions for purely electronic ferroelectricity from excitonic condensation and tested monolayer $Ta_2Pd_3Te_5$ against them. The band-edge order fails the polar condition, and the maximally localized Wannier Hamiltonian cannot test the dominance condition. This Hamiltonian of monolayer $Ta_2Pd_3Te_5$ retains only $\{E, 2_{1x}, \sigma_y, n_z\}$, the isotropy group of a polar B_{3u} order, because the unconstrained disentanglement selects a subspace with this symmetry and its Te p_x centres leave the mirror planes of their parent atoms. In this gauge the normal state is already polar, B_{3u} merges with the fully symmetric channel, and Wannier-centre polarizations are spurious, so channel energetics and polarizations of this family require a symmetry-adapted basis. Within the symmetry the Hamiltonian respects, the channel containing the band-edge A_u order[19] has the lowest critical coupling, 1.14–1.42 eV, above the 1.1 eV interaction of the bulk Hartree–Fock model[15]. The A_u state is nonpolar and chiral, with isotropy group $P2_12_12$; bulk observations, the mirror breaking detected by ARPES and $P2_12_12_1$ among the compatible subgroups, are consistent with it. Its linear coupling to silent A_u phonons makes a lattice distortion unavoidable. Band-edge excitonic pairing in this material therefore yields, for spin-singlet pairing, a chiral, nonpolar excitonic insulator rather than a pure electronic ferroelectric. The polar condition conflicts with the excitonic mechanism: the dipole-forbidden band edges that keep the attraction unscreened

are the ones that make the order nonpolar. A purely electronic excitonic ferroelectric requires a polar band-edge pair with a weak but nonzero interband dipole, or a polar channel that leads away from the band edges. Second-harmonic generation at normal incidence, shear-induced out-of-plane polarization and the Raman activation of the silent A_u phonons provide direct experimental tests.

Methods

Electronic structure

Density functional calculations use VASP[39] with projector augmented waves[40] and the r^{2}SCAN meta-GGA[23]; bulk calculations add the rVV10 nonlocal dispersion correction with $b = 11.95$ and $C = 0.0093$[24;41] for the interlayer binding. The plane-wave cutoff is 550 eV for the monolayer and the bulk. Bulk calculations start from the room-temperature single-crystal structure[14] and use a Γ-centred $7 \times 28 \times 5$ mesh. The monolayer is cut from the bulk and relaxed with r^{2}SCAN, without a dispersion correction because the isolated layer has no interlayer binding, in a cell with a 35 Å out-of-plane lattice parameter, giving $a = 3.753$ Å (chain axis, x) and $b = 18.668$ Å. The relaxed monolayer retains $Pmmn$ symmetry. For the bulk, r^{2}SCAN+rVV10 reproduces the normal-state ARPES dispersion (Supporting Information, Fig. S1).

Wannier Hamiltonian

A 16-orbital tight-binding Hamiltonian H_0 is constructed with Wannier90[28;42] from an r^{2}SCAN calculation on the full, symmetry-unreduced $28 \times 5 \times 1$ mesh, using four Ta d_{z^2}, ten Te p_x and two Pd d_{xz} projections, with disentanglement window $[-5.5, 1.3]$ eV, frozen window $[-3.1, -2.4]$ eV and guiding centres. The final spreads are 5.3–10.8 Å^2 (147 Å^2 in total). The frozen window ends 27 meV below the valence-band maximum, so the band-edge states are fixed by the disentanglement rather than frozen, and the 108 meV gap below is a property of the model; the DFT bands give a direct gap of 130 meV, with c_2 103 meV above c_1. Interband velocity matrix elements are evaluated from $\partial H_0/\partial \mathbf{k}$. With 12 occupied orbitals the model has a direct gap of 108 meV at Γ and contains 145 lattice vectors, all in plane. The symmetry-adapted model of the robustness test (Supporting Information, Sec. S4) is built with the Wannier90 site-symmetry option[29]

from a Quantum ESPRESSO calculation[43;44] with r^{2}SCAN evaluated through Libxc[45] and optimized norm-conserving Vanderbilt pseudopotentials[46] from the PseudoDojo table, generated with PBE[47].

Symmetry test of the Wannier Hamiltonian

Symmetry operators are constructed from the Wannier basis itself rather than tabulated. Each operation g of $Pmmn$ maps every Wannier centre onto a centre of the same orbital type up to a lattice vector, with the sign of the orbital under the rotation part of g; this defines a **k**-dependent signed permutation $U_g(\mathbf{k})$ (Supporting Information, Sec. S2). An operation is accepted as a symmetry of H_0 only if

$$r_g = \max_{\mathbf{k}} \left| U_g(\mathbf{k})\, H_0(\mathbf{k})\, U_g^{\dagger}(\mathbf{k}) - H_0(g\mathbf{k}) \right| < 20 \text{ meV}. \tag{2}$$

The residual is evaluated on the 36×8 mesh and along the X–Γ–Y path. The residuals are bimodal, at most 4.4 meV for the exact operations and at least 530 meV for the others. Because $H_0(\mathbf{k})$ is a finite Fourier series, $r_g \leq \sum_{\mathbf{R}} \max |\Delta_g(\mathbf{R})|$, where $\Delta_g(\mathbf{R})$ are the lattice Fourier coefficients of the residual matrix; this **k**-independent bound is at most 37 meV for the exact operations, so the classification holds at every **k**. The operations that pass, not the space group of the crystal, determine which irreducible representations a Wannier-based calculation can resolve. Irreducible representations follow the Bilbao conventions[48].

Channel-resolved instability

The excitonic field is defined on Ta–X bonds ($X =$ Te, Pd) within a cutoff r_c, not within the unit cell, because a cell-local field is not closed under the screw and glide operations of $Pmmn$. The field is projected only onto the irreducible representations of the subgroup that passes the symmetry test, so channels that H_0 cannot distinguish are never treated as separate. For each channel the critical coupling V_0^c of a bond-local electron–hole interaction V_0 is the inverse of the largest eigenvalue of the static $\mathbf{q} = 0$ pair susceptibility in that channel; it is independent of iteration mixing and starting guess, and self-consistent solutions confirm that the field vanishes below it. The formulation and convergence tests are given in the Supporting Information (Sec. S2). The model is spinless and describes spin-singlet pairing, as the bulk Hartree–Fock model of ref. 15; spin–orbit coupling

leaves the monolayer bands at Γ essentially unchanged in PBE, because the conduction-band edge is Ta d_{z^2} [19]. With spin, c_1 and c_2 are both Γ_5^- Kramers doublets, so spin–orbit coupling can mix them; it changes the band-edge gap by about 10 meV [19], small against $c_2 - c_1 = 103$ meV, so it alters the susceptibilities quantitatively but cannot make the A_u component polar. A spinful model with 32 Wannier functions would quantify the change. V_0 is an interaction per bond operator, so it is comparable in scale but not identical to the interaction $V = 1.1$ eV of the eight-orbital bulk Hartree–Fock model of Huang *et al.* [15]. V_0^c is a threshold for the screened interaction. Dielectric screening by a substrate weakens the effective interaction [49] and therefore moves the monolayer away from the instability; because all channels compete with the same bond interaction, a uniform reduction leaves their ordering unchanged, and the ordering is the same for the three bond sets of Fig. 5. The program (`ta2pd3te5_channel_mf_v6.py`) and its inputs are part of the data repository (Code availability).

Use of generative AI

During the preparation of this manuscript, the authors used Claude Opus 5.5 (Anthropic) to improve and debug the Python code for the analysis of the Wannier90 output, the tables and the figures, to detect anomalies in the data and text, to locate and summarize relevant publications, and to assist with drafting and language editing of the manuscript. No generative AI tools were used to create images; all figures were produced from the data with the published scripts or with VESTA [25]. The authors reviewed, validated and critically assessed all AI-assisted outputs and take full responsibility for the content of the manuscript.

Data availability

The Wannier90 Hamiltonians, Wannier90 input and output, VASP and Quantum ESPRESSO input files, the norm-conserving pseudopotentials of the Quantum ESPRESSO calculation, relaxed structures and all computed results and figures are openly available at `https://github.com/csonkagi/Ta2Pd3Te5-excitonic-ferroelectricity`. VASP pseudopotential files are not distributed owing to licence restrictions.

Code availability

The analysis code, including the symmetry test and channel-resolved mean-field program and the scripts that regenerate every table and figure, is available at `https://github.com/csonkagi/Ta2Pd3Te5-excitonic-ferroelectricity` under the MIT licence.

References

[1] D. Jérome, T. M. Rice, and W. Kohn. Excitonic insulator. *Phys. Rev.*, 158:462, 1967. doi: 10.1103/PhysRev.158.462.

[2] T. Portengen, Th. Östreich, and L. J. Sham. Theory of electronic ferroelectricity. *Phys. Rev. B*, 54:17452, 1996. doi: 10.1103/PhysRevB.54.17452.

[3] C. D. Batista. Electronic ferroelectricity in the Falicov-Kimball model. *Phys. Rev. Lett.*, 89: 166403, 2002. doi: 10.1103/PhysRevLett.89.166403.

[4] P. Monceau, F. Ya. Nad, and S. Brazovskii. Ferroelectric Mott-Hubbard phase of organic $(TMTTF)_2X$ conductors. *Phys. Rev. Lett.*, 86:4080, 2001. doi: 10.1103/PhysRevLett.86.4080.

[5] L. Zhang, J. Ding, H. Xiang, et al. Electronic ferroelectricity in monolayer graphene moiré superlattices. *Nat. Commun.*, 15:10905, 2024.

[6] R. Niu, Z. Li, X. Han, et al. Giant ferroelectric polarization in a bilayer graphene heterostructure. *Nat. Commun.*, 13:6241, 2022.

[7] X. Wang, G. Teng, X. Meng, Z. Cheng, T. Lin, H. Shen, X. Wang, J. Wang, and J. Chu. Is there a pure electronic ferroelectric? *Adv. Electron. Mater.*, page e00683, 2026.

[8] F. J. Di Salvo, D. E. Moncton, and J. V. Waszczak. Electronic properties and superlattice formation in the semimetal $TiSe_2$. *Phys. Rev. B*, 14:4321, 1976. doi: 10.1103/PhysRevB.14.4321.

[9] H. Cercellier et al. Evidence for an excitonic insulator phase in 1T-$TiSe_2$. *Phys. Rev. Lett.*, 99:146403, 2007. doi: 10.1103/PhysRevLett.99.146403.

[10] G. Mazza, M. Rösner, L. Windgätter, S. Latini, H. Hübener, A. J. Millis, A. Rubio, and A. Georges. Nature of symmetry breaking at the excitonic insulator transition: Ta_2NiSe_5. *Phys. Rev. Lett.*, 124:197601, 2020. doi: 10.1103/PhysRevLett.124.197601.

[11] E. Baldini et al. The spontaneous symmetry breaking in Ta_2NiSe_5 is structural in nature. *Proc. Natl. Acad. Sci. U.S.A.*, 120:e2221688120, 2023. doi: 10.1073/pnas.2221688120.

[12] A. Subedi. Orthorhombic-to-monoclinic transition in Ta_2NiSe_5 due to a zone-center optical phonon instability. *Phys. Rev. Mater.*, 4:083601, 2020. doi: 10.1103/PhysRevMaterials.4.083601.

[13] S. Bae, A. Raghavan, I. Feldman, A. Kanigel, and V. Madhavan. Microscopic evidence of dominant excitonic instability in Ta_2NiSe_5. arXiv:2512.03011, 2025.

[14] W. Tremel. Tetrahedral coordination of palladium in $Ta_2Pd_3Te_5$: a compound with a "stuffed" Ta_2NiSe_5 structure. *Angew. Chem. Int. Ed.*, 32:1752, 1993.

[15] J. Huang et al. Evidence for an excitonic insulator state in $Ta_2Pd_3Te_5$. *Phys. Rev. X*, 14:011046, 2024. doi: 10.1103/PhysRevX.14.011046.

[16] P. Zhang et al. Spontaneous gap opening and potential excitonic states in an ideal Dirac semimetal $Ta_2Pd_3Te_5$. *Phys. Rev. X*, 14:011047, 2024. doi: 10.1103/PhysRevX.14.011047.

[17] M. S. Hossain et al. Topological excitonic insulator with tunable momentum order. *Nat. Phys.*, 21:1250–1259, 2025.

[18] A. Wang et al. A robust and tunable Luttinger liquid in correlated edge of transition-metal second-order topological insulator $Ta_2Pd_3Te_5$. *Nat. Commun.*, 14:7647, 2023.

[19] J. Yao et al. Excitonic instability in $Ta_2Pd_3Te_5$ monolayer. *Chin. Phys. Lett.*, 41:097101, 2024. doi: 10.1088/0256-307X/41/9/097101.

[20] Z. Guo, J. Deng, Y. Xie, and Z. Wang. Quadrupole topological insulators in $Ta_2M_3Te_5$ (M = Ni, Pd) monolayers. *npj Quantum Mater.*, 7:87, 2022.

[21] Z. Guo, D. Yan, H. Sheng, S. Nie, Y. Shi, and Z. Wang. Quantum spin Hall effect in $Ta_2M_3Te_5$ (M = Pd, Ni). *Phys. Rev. B*, 103:115145, 2021. doi: 10.1103/PhysRevB.103.115145.

[22] Y.-S. Choi, D. Wulferding, R. Kalaivanan, R. K. Ulaganathan, R. Sankar, and K.-Y. Choi. Observation of an amplitudelike mode in the excitonic insulator $Ta_2Pd_3Te_5$. *Phys. Rev. Res.*, 8:023273, 2026. doi: 10.1103/2swg-p1pn.

[23] J. W. Furness, A. D. Kaplan, J. Ning, J. P. Perdew, and J. Sun. Accurate and numerically efficient r^2SCAN meta-generalized gradient approximation. *J. Phys. Chem. Lett.*, 11:8208, 2020. doi: 10.1021/acs.jpclett.0c02405.

[24] J. Ning et al. Workhorse minimally empirical dispersion-corrected density functional with tests for weakly bound systems: r^2SCAN+rVV10. *Phys. Rev. B*, 106:075422, 2022. doi: 10.1103/PhysRevB.106.075422.

[25] K. Momma and F. Izumi. VESTA 3 for three-dimensional visualization of crystal, volumetric and morphology data. *J. Appl. Crystallogr.*, 44:1272–1276, 2011. doi: 10.1107/S0021889811038970.

[26] R. W. Boyd. *Nonlinear Optics*. Academic Press, London, 4th edition, 2020.

[27] J. Xiao, H. Zhu, Y. Wang, W. Feng, Y. Hu, A. Dasgupta, Y. Han, Y. Wang, D. A. Muller, L. W. Martin, P. Hu, and X. Zhang. Intrinsic two-dimensional ferroelectricity with dipole locking. *Phys. Rev. Lett.*, 120:227601, 2018. doi: 10.1103/PhysRevLett.120.227601.

[28] N. Marzari, A. A. Mostofi, J. R. Yates, I. Souza, and D. Vanderbilt. Maximally localized Wannier functions: theory and applications. *Rev. Mod. Phys.*, 84:1419, 2012. doi: 10.1103/RevModPhys.84.1419.

[29] R. Sakuma. Symmetry-adapted Wannier functions in the maximal localization procedure. *Phys. Rev. B*, 87:235109, 2013. doi: 10.1103/PhysRevB.87.235109.

[30] R. D. King-Smith and D. Vanderbilt. Theory of polarization of crystalline solids. *Phys. Rev. B*, 47:1651, 1993. doi: 10.1103/PhysRevB.47.1651.

[31] B. I. Halperin and T. M. Rice. The excitonic state at the semiconductor–semimetal transition. In F. Seitz, D. Turnbull, and H. Ehrenreich, editors, *Solid State Physics*, volume 21, pages 115–192. Academic Press, New York, 1968.

[32] J. Kuneš. Excitonic condensation in systems of strongly correlated electrons. *J. Phys.: Condens. Matter*, 27:333201, 2015. doi: 10.1088/0953-8984/27/33/333201.

[33] H. Katsura, N. Nagaosa, and A. V. Balatsky. Spin current and magnetoelectric effect in noncollinear magnets. *Phys. Rev. Lett.*, 95:057205, 2005. doi: 10.1103/PhysRevLett.95.057205.

[34] H. Tang, J. Wei, G. I. Csonka, and A. Ruzsinszky. Diverse edge and excitonic states of $Ta_2Ni_3Te_5$ nanoribbons and monolayer: implications for nanoelectronics. *ACS Appl. Nano Mater.*, 9:16038, 2026. doi: 10.1021/acsanm.6c02920.

[35] K. Harrison, D. A. Jeff, J. M. DeStefano, O. Peek, A. Kushima, J.-H. Chu, H. R. Gutiérrez, and S. I. Khondaker. In-plane anisotropy in the layered topological insulator $Ta_2Ni_3Te_5$ investigated via TEM and polarized Raman spectroscopy. *ACS Nano*, 18:4811–4821, 2024. doi: 10.1021/acsnano.3c09527.

[36] Z. Sun, Z. Guo, D. Yan, P. Cheng, L. Chen, Y. Shi, Y. Huang, Z. Wang, K. Wu, and B. Feng. Layer-dependent Raman spectroscopy of ultrathin $Ta_2Pd_3Te_5$. *Phys. Rev. Mater.*, 7:094004, 2023.

[37] M. Iraola et al. IrRep: symmetry eigenvalues and irreducible representations of ab initio band structures. *Comput. Phys. Commun.*, 272:108226, 2022. doi: 10.1016/j.cpc.2021.108226.

[38] WannierBerri developers. WannierBerri documentation. Online documentation, 2026. URL `https://docs.wannier-berri.org`. Accessed 30 October 2026.

[39] G. Kresse and J. Furthmüller. Efficient iterative schemes for ab initio total-energy calculations using a plane-wave basis set. *Phys. Rev. B*, 54:11169, 1996. doi: 10.1103/PhysRevB.54.11169.

[40] G. Kresse and D. Joubert. From ultrasoft pseudopotentials to the projector augmented-wave method. *Phys. Rev. B*, 59:1758, 1999. doi: 10.1103/PhysRevB.59.1758.

[41] R. Sabatini, T. Gorni, and S. de Gironcoli. Nonlocal van der Waals density functional made simple and efficient. *Phys. Rev. B*, 87:041108(R), 2013. doi: 10.1103/PhysRevB.87.041108.

[42] G. Pizzi et al. Wannier90 as a community code: new features and applications. *J. Phys.: Condens. Matter*, 32:165902, 2020. doi: 10.1088/1361-648X/ab51ff.

[43] P. Giannozzi et al. QUANTUM ESPRESSO: a modular and open-source software project for quantum simulations of materials. *J. Phys.: Condens. Matter*, 21:395502, 2009. doi: 10.1088/0953-8984/21/39/395502.

[44] P. Giannozzi et al. Advanced capabilities for materials modelling with Quantum ESPRESSO. *J. Phys.: Condens. Matter*, 29:465901, 2017. doi: 10.1088/1361-648X/aa8f79.

[45] S. Lehtola, C. Steigemann, M. J. T. Oliveira, and M. A. L. Marques. Recent developments in Libxc: a comprehensive library of functionals for density functional theory. *SoftwareX*, 7: 1–5, 2018. doi: 10.1016/j.softx.2017.11.002.

[46] D. R. Hamann. Optimized norm-conserving Vanderbilt pseudopotentials. *Phys. Rev. B*, 88: 085117, 2013. doi: 10.1103/PhysRevB.88.085117.

[47] M. J. van Setten, M. Giantomassi, E. Bousquet, M. J. Verstraete, D. R. Hamann, X. Gonze, and G.-M. Rignanese. The PseudoDojo: Training and grading a 85 element optimized norm-conserving pseudopotential table. *Comput. Phys. Commun.*, 226:39–54, 2018. doi: 10.1016/j.cpc.2018.01.012.

[48] M. I. Aroyo et al. Bilbao Crystallographic Server: I. Databases and crystallographic computing programs. *Z. Kristallogr.*, 221:15, 2006. doi: 10.1524/zkri.2006.221.1.15.

[49] L. V. Keldysh. Coulomb interaction in thin semiconductor and semimetal films. *JETP Lett.*, 29:658, 1979.

Acknowledgements

H.T. was supported by the Department of Energy Office of Basic Sciences under grant no. DE-SC0018331. A.R. acknowledges the U.S. Department of Energy, Office of Science, Office of Basic

Energy Sciences, under Award Number DE-SC0026293.

Author contributions

G.I.C. conceived the project, developed the symmetry analysis and the channel-resolved mean-field code, and wrote the manuscript. H.T. prepared the input files, ran the density functional (VASP and Quantum ESPRESSO) and Wannier90 calculations, provided the output for analysis and identified the reduced symmetry of the Wannier centres. A.R. contributed to the conception of the project and the interpretation of the results. All authors discussed the results and revised the manuscript.

Competing interests

The authors declare no competing interests.

Supplementary Files

This is a list of supplementary files associated with this preprint. Click to download.

- SI.pdf